

# A Surface Modification Strategy Towards Reversible Na-ion Intercalation on Graphitic Carbon Using Fluorinated Few-Layer Graphene

To cite this article: Dipobrato Sarbapalli et al 2022 J. Electrochem. Soc. 169 106522

View the article online for updates and enhancements.







# A Surface Modification Strategy Towards Reversible Na-ion Intercalation on Graphitic Carbon Using Fluorinated Few-Layer Graphene

Dipobrato Sarbapalli, <sup>1,\*\*</sup> <sup>®</sup> Yu-Hsiu Lin, <sup>2</sup> <sup>®</sup> Sean Stafford, <sup>3</sup> <sup>®</sup> Jangyup Son, <sup>4,a</sup> Abhiroop Mishra, <sup>1,\*\*</sup> <sup>®</sup> Jingshu Hui, <sup>1,b</sup> <sup>®</sup> A Nijamudheen, <sup>2,c</sup> <sup>®</sup> Adolfo I. B. Romo, <sup>1</sup> <sup>®</sup> Zachary T. Gossage, <sup>1,d</sup> <sup>®</sup> Arend M. van der Zande, <sup>4</sup> <sup>®</sup> Jose L. Mendoza-Cortes, <sup>2,3,z</sup> <sup>®</sup> and Joaquín Rodríguez-López <sup>1,\*,z</sup> <sup>®</sup>

Na-ion batteries (NIBs) are proposed as a promising candidate for *beyond* Li-ion chemistries, however, a key challenge associated with NIBs is the inability to achieve intercalation in graphite anodes. This phenomenon has been investigated and is believed to arise due to the thermodynamic instability of Na-intercalated graphite. We have recently demonstrated theoretical calculations showing it is possible to achieve thermodynamically stable Na-intercalated graphene structures with a fluorine surface modifier. Here, we present experimental evidence that  $Na^+$  intercalation is indeed possible in fluorinated few-layer graphene (F-FLG) structures using cyclic voltammetry (CV), ion-sensitive scanning electrochemical microscopy (SECM) and in situ Raman spectroscopy. SECM and Raman spectroscopy confirmed  $Na^+$  intercalation in F-FLG, while CV measurements allowed us to quantify Na-intercalated F-FLG stoichiometries around  $NaC_{14-18}$ . These stoichiometries are higher than the previously reported values of  $NaC_{186}$  in graphite. Our experiments revealed that reversible  $Na^+$  ion intercalation also requires a pre-formed Li-based SEI in addition to the surface fluorination, thereby highlighting the critical role of SEI in controlling ion-transfer kinetics in alkaliion batteries. In summary, our findings highlight the use of surface modification and careful study of electrode-electrolyte interfaces and interphases as an enabling strategy for NIBs.

© 2022 The Electrochemical Society ("ECS"). Published on behalf of ECS by IOP Publishing Limited. [DOI: 10.1149/1945-7111/ac9c33]

Manuscript submitted August 19, 2022; revised manuscript received October 5, 2022. Published October 31, 2022.

Supplementary material for this article is available online

The demand for Li-ion batteries (LIBs) is ever increasing owing to their beneficial performance and cost characteristics for applications ranging from consumer electronics to vehicular transportation.<sup>1</sup> However, research into the Li raw material reserves are predicting shortages, <sup>3</sup> along with limitations on logistics associated with LIB supply chains. <sup>2,4,5</sup> Therefore, *beyond* Li-ion chemistries are attracting increased attention, <sup>4,6–8</sup> along with different battery architectures such as flow batteries. Some examples of these beyond Li-ion battery technologies include Na-ion (NIB) and K-ion battery (KIB) chemistries. Focusing specifically on NIBs, Yabuuchi et al.,8 comprehensively reviewed developments in the field and highlighted the importance of NIBs over LIBs, including (i) widespread abundance and consequently, low cost of sodium, (ii) comparable theoretical capacities, (iii) and weaker desolvation energies associated with Na<sup>+</sup>, leading to energetically beneficial intercalation processes and solid state Na<sup>+</sup> diffusion, among others.<sup>6,9</sup> Thus, there is potential of NIBs being a candidate for practical beyond Li-ion battery technologies. 10

Current Na-ion batteries utilize intercalation electrodes; cathodes are based on transition metal oxides which are structurally similar to LIB cathodes (for example those based on O3-type NaMO<sub>2</sub> crystal

structures, where M represents certain transition metals)<sup>11,12</sup> among others such as Prussian Blue. <sup>13</sup> On the anode side, unlike LIBs, NIBs utilize use hard/non-graphitizable carbons with reversible capacities >200 mAh g<sup>-1</sup>. <sup>14–16</sup> However, hard carbons are influenced by their source materials and preparation method and can show large irreversible capacities during initial cycles. <sup>17</sup> Commercial LIBs utilize either natural or artificial forms of graphite as the anode material, owing to its high storage capacity and excellent (de) intercalation characteristics. <sup>18</sup> Given the well-established use of graphite in a commercial LIB battery, it is desirable to use the same materials and open a new field of anode materials of NIBs. This point is even more critical because implementing alternative Na-metal anodes currently face challenges owing to high reactivity, leading to unstable solid-electrolyte interphases and dendrite growth. <sup>19,20</sup>

However, one of the major issues for extending the use of graphite to NIB anodes is the low Na<sup>+</sup> storage capacity within graphitic carbons. Dahn and co-workers reported graphite to be a poor intercalation host for Na<sup>+</sup> ions, with the experimentally measured stoichiometry being NaC<sub>186</sub>,<sup>21</sup> compared to the LiC<sub>6</sub> or LiC<sub>8</sub> stoichiometries in LIBs.<sup>22</sup> Subsequently, it has been reported that the origin of poor intercalation capacity stems from unfavorable interactions between intercalated Na and C atoms in graphite. 25,26 We hypothesized that these unfavorable interactions could be overturned by using 2D materials with distinct surface electronic properties that create the conditions for Na+ intercalation.<sup>24</sup> Thus, we recently presented theoretical calculations<sup>24</sup> which highlighted that a fluorine surface modifier built over a thin, 4layer graphene structure resulted in thermodynamically favorable Na<sup>+</sup> intercalated structures. Experimental realization of this theoretical work could have significant impacts on the fundamental understanding of Na<sup>+</sup> intercalation in graphitic carbons. Therefore, the scope of this paper is focused on the experimental investigation of Na<sup>+</sup> intercalation in modified CVD-grown few-layer graphene (FLG) structures. Fluorine

<sup>&</sup>lt;sup>1</sup>Department of Chemistry, University of Illinois at Urbana-Champaign, Urbana, Illinois 61801, United States of America <sup>2</sup>Department of Chemical Engineering & Materials Science, Michigan State University, East Lansing, Michigan 48824, United States of America

<sup>&</sup>lt;sup>3</sup>Department of Physics, College of Arts and Science, Florida State University, Tallahassee, Florida 32306, United States of America

<sup>&</sup>lt;sup>4</sup>Department of Mechanical Science and Engineering, University of Illinois at Urbana-Champaign, Urbana, Illinois 61801, United States of America

<sup>\*</sup>Electrochemical Society Member.

<sup>\*\*</sup>Electrochemical Society Student Member.

<sup>&</sup>lt;sup>a</sup>Present address: Functional Composite Materials Research Center, Korea Institute of Science and Technology, Jeonbuk 55324, South Korea.

bPresent address: College of Energy, Soochow Institute for Energy and Materials InnovationS (SIEMIS), Key Laboratory of Advanced Carbon Materials and Wearable Energy Technologies of Jiangsu Province, Soochow University, Suzhou, 215006 P. R. China.

<sup>&</sup>lt;sup>c</sup>Present address: Inorganic Chemistry Laboratory, University of Oxford, South Parks Rd, Oxford OX1 3QR, United Kingdom.

<sup>&</sup>lt;sup>d</sup>Present address: Department of Applied Chemistry, Tokyo University of Science, Shinjuku, Tokyo 162–8601, Japan.

<sup>&</sup>lt;sup>z</sup>E-mail: jmendoza@msu.edu; joaquinr@illinois.edu

surface modification on FLG (F-FLG) was achieved by exposure to XeF<sub>2</sub> gas. <sup>27,28</sup> We utilized cyclic voltammetry (CV), ion-sensitive scanning electrochemical microscopy (SECM), and in situ Raman spectroscopy to probe Na<sup>+</sup> charge storage capacity and associated mechanisms in F-FLG electrodes. Finally ex situ scanning electron microscopy (SEM) and X-ray photoelectron spectroscopy (XPS) were performed to characterize interphases forming on these F-FLG electrodes. Our results revealed that Na<sup>+</sup> intercalation takes place with reversible stoichiometries higher than previously reported using a modified interface and SEI, seeding new directions for developing graphitic carbons as NIB anodes.

#### **Methods and Materials**

Chemicals.—All chemicals were purchased from commercial sources and used as received. Propylene carbonate (PC, anhydrous, 99.7%), ethylene carbonate (EC, anhydrous, 99%), lithium tetrafluoroborate (LiBF<sub>4</sub>, 98%), ferrocene (Fc, 98%), acetone (99.5%), isopropyl alcohol (IPA 99.5%), glacial acetic acid (99.5%), N, N, N', N'-tetramethyl-p-phenylenediamine (TMPD, 99%) and ethylenediaminetetraacetic acid disodium salt dihydrate (Na<sub>2</sub>EDTA·2H<sub>2</sub>O, 99.0%), Poly (Bisphenol A carbonate), with an average Mw of 45000, were all purchased from Sigma-Aldrich. Tetrakis(decyl) ammonium hexafluorophosphate (TkDAPF<sub>6</sub>) was synthesized in house using tetrakis(decyl)ammonium bromide (99%, TCI) and silver hexafluorophosphate (98%, Sigma); synthesis and characterization is reported in section S1 of SI. 25  $\mu$ m thick copper foil was purchased from Alfa Aesar. Copper etchant was purchased from Transene Company. SiO<sub>2</sub>/Si wafer (3 in. B-doped P-type Si wafer with 300 nm wet thermal oxide) was purchased from University Wafer.

FLG synthesis, transfer, and fluorination.—FLG was synthesized through chemical vapor deposition (CVD) on pretreated copper foil catalyst following previously reported procedures.<sup>29–3</sup> The Cu foil was treated in solvents in the following order, to remove any organic contaminants and surface oxides: acetone (10 s), water (10 s), glacial acetic acid (10 min), water (10 s), acetone (10 s), and IPA (10 s). FLG was grown on Cu foil in a quartz tube, under atmospheric pressure at 960 °C (Ramp time from room temperature to 960 °C in 1.5 h), 10 seem CH<sub>4</sub> and 30 secm H<sub>2</sub> for 2.5 min. FLG was transferred on SiO<sub>2</sub>/Si wafer and quartz coverslips through a wet transfer method,<sup>32</sup> using poly(bisphenol A carbonate). After Cu etching, transfer steps involved four rinsing steps floating the FLG on DI water, 2 h treatment with 0.1 M Na<sub>2</sub>EDTA aqueous solution, and four additional rinse steps with DI water again to fully remove any metal residue. After transfer to Pt padded SiO2/Si wafer (for mitigating conductivity issues in fluorinated FLG, section S2, SI) and drying in a vacuum desiccator, samples were immersed in chloroform overnight to remove the polycarbonate protecting layer. For FLG fluorination, we used a XeF2 etcher (Xactix etching system) with expansion chamber partial pressure of XeF2 set to 3 torr at room temperature. We exposed the FLG over 12 cycles of fresh XeF<sub>2</sub> at 1.3 torr specimen chamber pressure for 30 s each cycle. Fluorination extent was ~56%, as characterized using single layer graphene as proxy (Fig. S2).

Graphene characterization.—FLG was characterized through SEM, Raman spectroscopy and transmittance microscopy. The absorbance of graphene to radiation between 500–700 nm wavelengths is known to be 2.3% per layer. Transmittance micrographs (Fig. 1a) obtained at 561 nm was subsequently used to obtain layer number distribution maps (Fig. 1b). SEM of FLG (Fig. 1c) was performed on a Hitachi S4800 field emission microscope. Raman spectral maps were collected using a Nanophoton Laser Raman Microscope (RAMAN-11, Japan). XPS was performed using a Kratos Axis Ultra X-ray photoelectron spectrometer. Resulting characterization of FLG graphene is shown in Fig. 1.

Figures 1b, 1d and 1e illustrate heterogeneity in terms of grain sizes and layer numbers, leading to the presence of edge planes and grain boundaries in the FLG structure. The presence of edge planes and grain boundaries is critical for the electrochemical intercalation experiments. This is because, ion intercalation primarily occurs through edge planes, as demonstrated in earlier work for similar graphitic carbon films. PXPS spectra confirm the fluorination of FLG (Fig. 1f), with the trend of decreased Raman 2D peak intensity and increased D peak intensity (Fig. 1g) agreeing with those observed in literature for the fluorination of graphene materials. PARS 34

Electrochemical methods.—Cyclic voltammetry and galvanostatic cycling were performed in a VTI glovebox (O<sub>2</sub>, H<sub>2</sub>O <1 ppm) using a CHI 760E potentiostat. The graphene electrodes were assembled in an open Teflon cell with Viton o-rings to isolate a 3 mm region ( $\sim$ 7.1 mm<sup>2</sup> area) and flooded with  $\sim$ 1 ml of electrolyte for measurements. 0.1 M LiBF<sub>4</sub> in 1:1 PC-EC (propylene carbonate: ethylene carbonate, by vol, henceforth referred as Li electrolyte solution) was used to form the Li-SEI on FLG electrodes. For Na<sup>+</sup> intercalation experiments we used 0.1 M NaPF<sub>6</sub> in 1:1 PC-EC (by vol., henceforth referred as Na electrolyte solution). The choice of 0.1 M LiBF<sub>4</sub> was made on the basis of previous work in our group, <sup>29–31</sup> which highlights stable cyclability and SEI formation capabilities of the electrolyte. To maintain concentration comparisons, we subsequently chose 0.1 M NaPF<sub>6</sub> for investigating Na<sup>+</sup> intercalation. All measurements were performed with a polypyrrole quasi-reference<sup>35,36</sup> (PPyQRE) given Na-metal references can interfere in electrochemical measurements,<sup>37</sup> and 0.5 mm dia. Pt wire as counter electrode. The PPyQRE reference potential was calibrated to ferrocene (Fc/Fc<sup>+</sup>) externally, using the same solution as that used in the experiment (albeit with the addition of  $\sim$ 1 mM Fc). Ion-sensitive SECM measurements used a CHI-920D bipotentiostat, with an Ag wire as quasi-reference, and Pt wire as counter electrode. Potentials were calibrated internally and reported vs ferrocene. Potentials in the in situ Raman measurements were calibrated by adding ferrocene internally, after all Raman measurements were completed. All electrochemical measurements on graphene inside a glovebox were replicated across multiple samples to ensure reproducibility. In situ Raman measurements were performed at two spots within a single experiment using a Horiba LabRAM HR 3D spectrometer, with a 532 nm laser operating at a power level of  $\sim$ 1.5 mW. Spectra were collected with 3 s exposure, with an average of 3 scans measured. These conditions translate to acquisition of Raman spectra every 75 mV during in situ Raman experiments coupled with CV.

Fabrication of Hg probes for ion-sensitive SECM.—Spherecapped Hg-UMEs (HgSC, Fig. S3) were prepared following previous work.  $^{38,39}$  25  $\mu m$  diameter Pt UMEs were sharpened, polished and etched while sonicating in a saturated CaCl2/HCl solution by applying an AC waveform with a peak-to-peak voltage of 2.7 V using a Variac transformer and a graphite counter electrode. Probes were etched for 30 s followed by sonication in DI water. Hg was electrodeposited at 0 V vs Ag/AgCl from a 10 mM solution of Hg(NO<sub>3</sub>)<sub>2</sub>.6H<sub>2</sub>O with 0.1 M KNO<sub>3</sub> supporting electrolyte.

*X-ray photoelectron spectroscopy (XPS).*—Prior to XPS analysis, samples were dried inside the box, followed by rinsing with IPA and drying in air. The XPS measurements were performed with a Kratos Axis Ultra electron spectrometer, using monochromated Al K $\alpha$  radiation (1486.6 eV). Survey spectra were recorded at energy resolution of 1 eV, pass energy 160 eV and high-resolution spectra for individual elements recorded at 0.1 eV, pass energy 40 eV. The area interrogated was 0.3 mm  $\times$  0.7 mm. All spectra were calibrated to 284.4 eV C–C peak for graphite, and peak fitting was performed using CasaXPS v2.3.22. Voigt peaks of a Gaussian/Lorentzian product form with 30% Lorentzian mix factor (GL 30) was used as the line shape for the peak fitting, along with Shirley background.

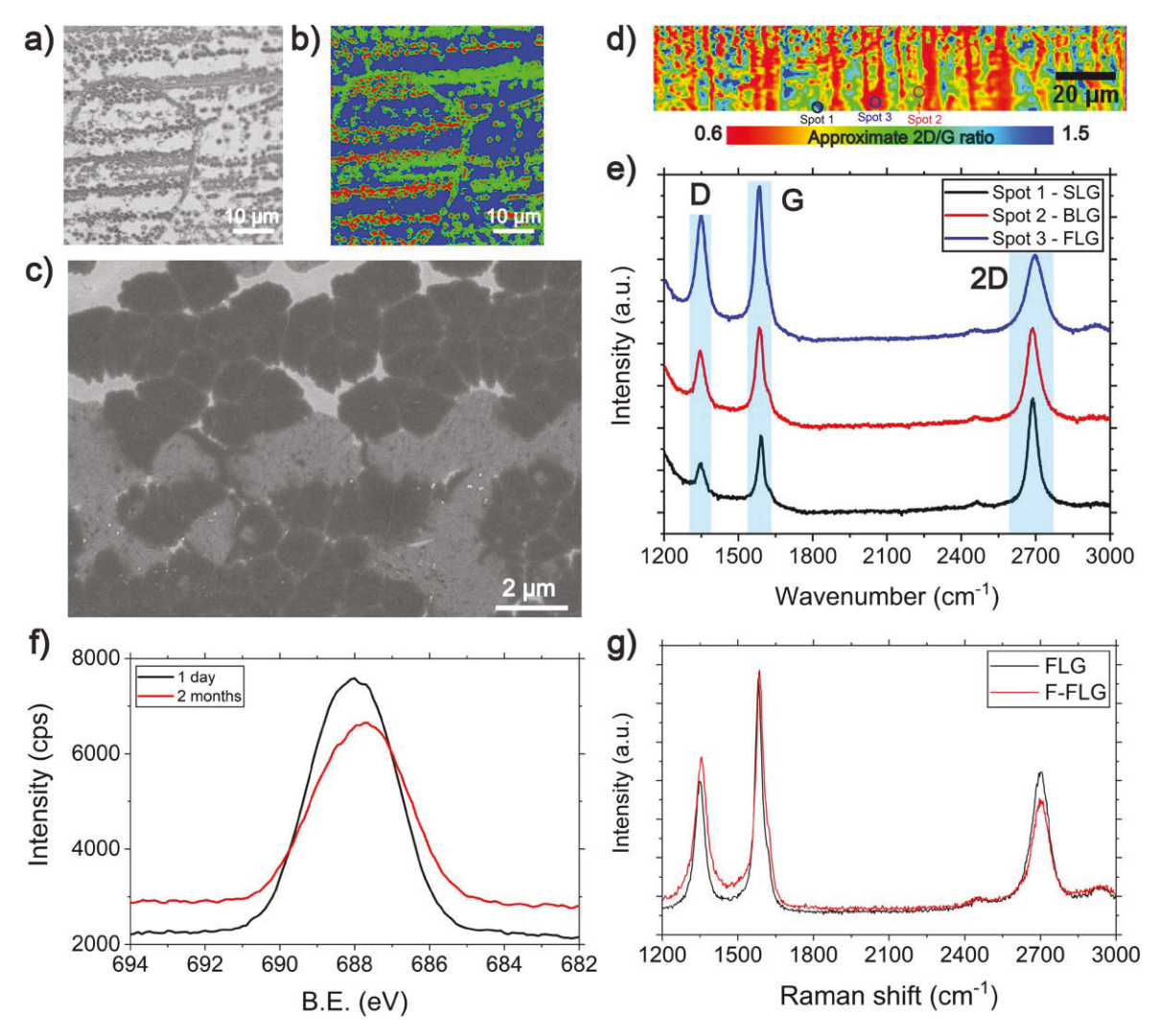


Figure 1. Characterization of FLG samples. (a) Transmittance micrograph of FLG on borosilicate coverslips obtained with 561 nm laser, and (b) corresponding layer number distribution map.  $\sim$ 48% area is <5 layers. (c) SEM micrograph of FLG illustrating grain sizes  $\sim$ 1  $\mu$ m. (d) Raman map illustrating approximate 2D/G ratios (calculated without baseline correction) across the sample, with (e) areas highlighting single layer graphene (SLG), bilayer graphene (BLG) and few-layer graphene (FLG). D, 2D and G peak is illustrated in (e). (f) XPS F 1 s spectra of F-FLG after storage in Ar-glovebox for 1 day and 2 months. (g) Raman spectra comparing FLG and F-FLG.

The C–C peak was fit with a GL30 peak shape modified with an asymmetric tail function  $A(0.5,\,0.15,\,0)$  in CasaXPS software.

Computational details.—We performed geometry optimizations and Raman frequency calculations on FLG structures of varying intercalation stages with and without a fluorine-attached surface modifier (See section S3 and Figs. S4-S9). Each structure was treated as a slab, that is, a large vacuum of  ${\sim}500~\text{Å}$  was included to prevent interactions between adjacent unit cells. We performed the quantum calculations at the hybrid density functional theory (DFT) level, as implemented in the CRYSTAL17 code. 40,41 CRYSTAL17 implements hybrid DFT using atom-centered Gaussian-type functions. These functions solve Hartree-Fock terms efficiently and enable quick computation of hybrid DFT density. Note that the Gaussian-type functions also permitted our large spacing between slabs which is different that codes using plane-waves as basis sets. Our calculations approximated the exchange-correlation with the Becke, 3-parameter, Lee-Yang-Parr (B3LYP)<sup>42</sup> functional. We included spin-polarization effects (unrestricted) and DFT-D3<sup>43</sup> corrections with Becke-Jonson damping<sup>44</sup> to account for dispersive interactions. We represented the orbitals of carbon, fluorine, and sodium with Gaussian basis sets with triple-zeta valence quality.<sup>45</sup> Self-consistent field (SCF) convergence was accelerated with the direct inversion of invariant subspace (DIIS),  $^{46,47}$  otherwise known as Pulay mixing, which constructs charge density from a linear combination of previous charge densities. The reciprocal space for all the structures was sampled by a  $\Gamma$ -centered Monkhorst-Pack scheme with a resolution of around  $2\pi \times 1/60~\text{Å}^{-1}$  (a. $k_a = 40$ –60, b. $k_b = 40$ –60,  $k_c = 1$ ). We initially optimized geometry with one set of convergence criteria (see S3.1) and then used stricter criteria during frequency calculations. Vibrational modes are calculated using second derivatives of density, so they depend sensitively upon the potential energy surface and hence demand increased stringency. These stricter frequency calculation criteria included an SCF energy convergence criterion of  $2.72 \times 10^{-10}~\text{eV}$ , an RMS force criterion of  $1.54 \times 10^{-3}~\text{eV}~\text{Å}^{-1}$ , a max force criterion of  $2.31 \times 10^{-3}~\text{eV}~\text{Å}^{-1}$ , an RMS displacement of  $6.35 \times 10^{-5}~\text{Å}$ , a max displacement criterion of  $9.53 \times 10^{-5}~\text{Å}$  and a between-geometry energy convergence criterion of  $2.72 \times 10^{-9}~\text{Å}$ . We optimized both atomic positions and unit cell parameters during frequency calculations.

# **Results and Discussion**

First, we utilized CV to characterize the Li<sup>+</sup> intercalation characteristics of F-FLG anodes. Figure 2a reveals that Li<sup>+</sup> (de) intercalation follows a well characterized staging mechanism displaying multiple peaks, and its behavior is similar to those reported

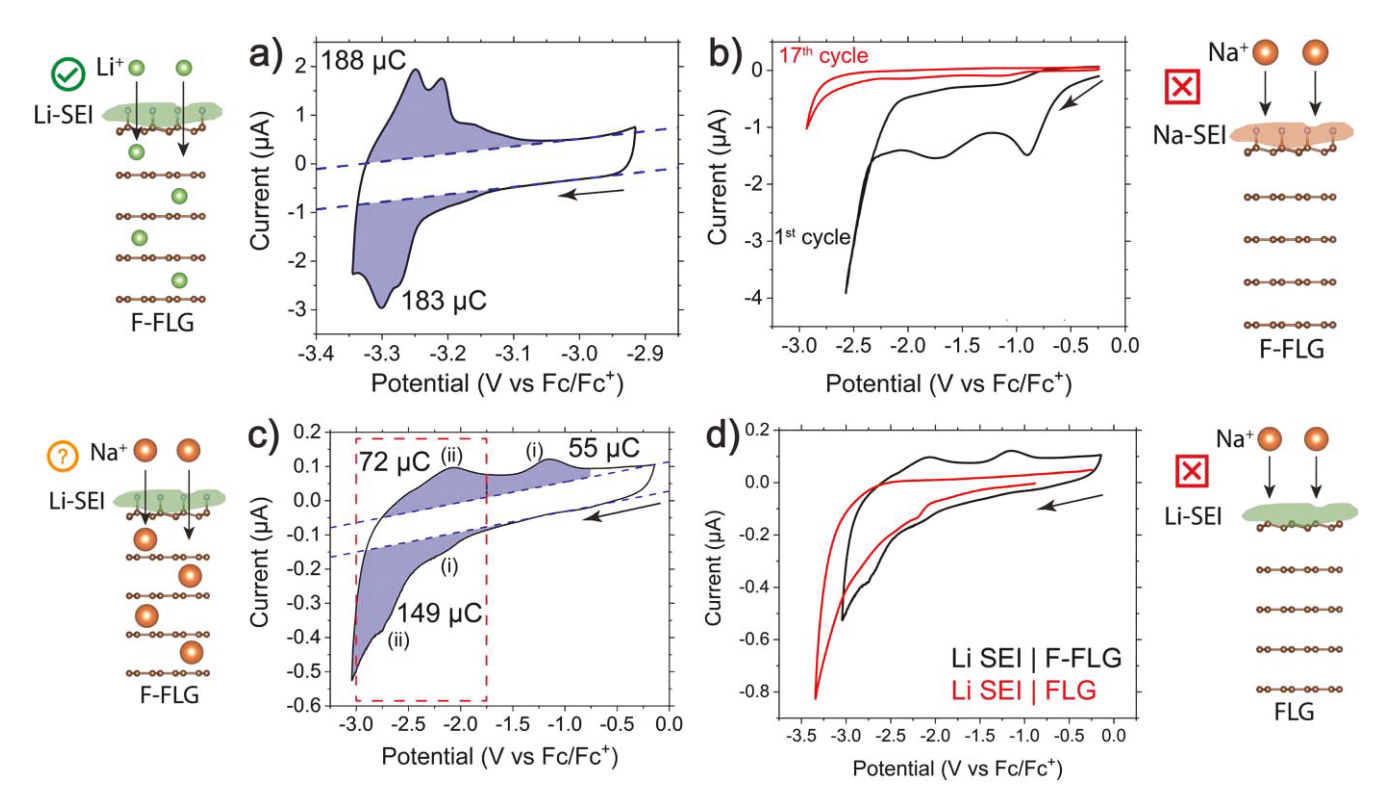


Figure 2. CV of F-FLG samples under different conditions, along with interpretations depicted by adjacent schemes. (a) Cycling F-FLG in 0.1 M LiBF<sub>4</sub> revealing clear staging peaks associated with Li<sup>+</sup> (de)intercalation. (b) Cycling F-FLG in 0.1 M NaPF<sub>6</sub> reveals no reversible peaks. (c) Cycling F-FLG with preformed Li-SEI (formed by CV, refer Fig. S12) in Na-electrolyte reveals reversible peaks, marked as i, ii. The red box highlights the potential regime associated with peak ii, which will be discussed later. (d) Comparison between F-FLG and FLG samples with preformed Li SEI, cycled in Na-electrolyte. All CVs at 1 mV s<sup>-1</sup>,  $\sim$ 7.1 mm<sup>2</sup> electrode area.

in few and multi-layer graphene samples.<sup>29-31</sup> With the knowledge that the F-FLG is a suitable Li<sup>+</sup> intercalation host, we attempted Na<sup>+</sup> intercalation via CV at 1 mV s<sup>-1</sup>, as shown in Fig. 2b in a solution of 0.1 M NaPF<sub>6</sub> dissolved in 1:1 PC-EC. All potentials were calibrated to the ferrocene redox couple unless stated otherwise. The first CV cycle revealed irreversible peaks between -1 to -2 V and beyond -2.5 V, likely associated with solid electrolyte interphase (SEI) formation processes. Further cycling in a shorter potential window reduces the current intensities at -1.25 V (Fig. S10), indicating that the resulting interphases are passivating in nature. Once the currents decreased by an order of magnitude, CV in an extended potential window did not reveal reversible intercalation signatures, despite what was reported previously in our simulations.<sup>24</sup> SEM and XPS characterization on the resulting interphase structures revealed a dense layer of inorganic species on the surface of F-FLG, primarily attributed to the formation of NaF, Fig. S11).

These observations imply that despite the calculations predicting thermodynamic stability of Na<sup>+</sup> intercalated graphene structures, the kinetics of the electrochemical intercalation process may be critical in achieving reversible intercalation. A similar observation was made for K<sup>+</sup> intercalation in FLG, wherein our group reported that a preformed Li-based SEI drastically improved K<sup>+</sup> intercalation kinetics.<sup>31</sup> Therefore, we hypothesized that the Na<sup>+</sup> intercalation may be impeded due to the properties of the SEI being formed on the F-FLG in Na- electrolyte. Subsequently, we explored Na<sup>+</sup> intercalation behavior in F-FLG samples with a preformed Li-based SEI.

For these measurements, we started with a F-FLG sample assembled in an open cell flooded with Li electrolyte. Li-based SEIs were formed by cycling the electrode in three different potential windows consecutively, as shown in Fig. S12. Subsequently, the Li-electrolyte was taken out, and the cell was rinsed 8 times with PC. We also soaked the cell in PC for 15 min to remove any residual salt from 0-rings in the last two steps. Prior to cycling in NaPF<sub>6</sub> electrolyte, we cycled the electrode in 10 mM

TkDAPF<sub>6</sub>, which lacks an alkali ion to intercalate, to rule out the presence of active Li<sup>+</sup> in the solution or in the SEI which could intercalate into FLG, as shown in Fig. S13. With these procedures, CVs in Na electrolyte, illustrated in Fig. 2c, displayed two reversible but broad peaks (i) and (ii). These peaks, which were observed at a significantly different potential compared to Li+ intercalation strongly suggest a reversible electrochemical process taking place. No such reversible peaks were observed when cycling pristine F-FLG samples in Na-electrolyte (Fig. S14). The baseline-corrected discharge capacity for F-FLG anode (Fig. 2c), corresponding to peak (i) and (ii) was calculated to be 55  $\mu$ C (between -1.75 and -0.75 V) and 72  $\mu$ C (between -2.75 and -1.75 V) respectively. Repeat experiments on other F-FLG samples revealed that peak (i) is not always observable, and therefore, we consider the discharge capacity to be 72  $\mu$ C, assuming that this value corresponds to reversible intercalation, as discussed below. For correlation to subsequent experiments, we have marked the potential regime (-1.75 to) $-3.0 \,\mathrm{V}$ ) associated with this reversible charge storage process with a red dashed box.

The discharge capacity of Li<sup>+</sup> in this sample was observed to be 188  $\mu C$  (Fig. 2a),  $\sim 3$  times more than the Na<sup>+</sup> capacity. Assuming this charge capacity corresponds to LiC<sub>6</sub>,  $^{31}$  the equivalent Na<sup>+</sup> stoichiometry is around NaC<sub>14</sub>. This Na-intercalated stoichiometry corresponds to a gravimetric capacity 159 mAh g $^{-1}$ . Repeat measurements on other F-FLG samples with galvanostatic cycling yielded discharge capacities of 150 and 50  $\mu C$  in 0.1 M LiBF<sub>4</sub> and NaPF<sub>6</sub> respectively, shown in Fig. S15. The resulting equivalent stoichiometry is  $\sim$  NaC<sub>18</sub>, consistent with the CV charge capacity calculations. Therefore, reversible charge storage is confirmed to be taking place at stoichiometries far exceeding the previously reported value of NaC<sub>186</sub>, in graphitic electrodes. The stoichiometry reported in our work also exceeds the reported values of NaC<sub>64–96</sub> for chemically intercalated Na<sup>+</sup> in carbon. However, from this data it is difficult to discern if the charge storage follows a staging-

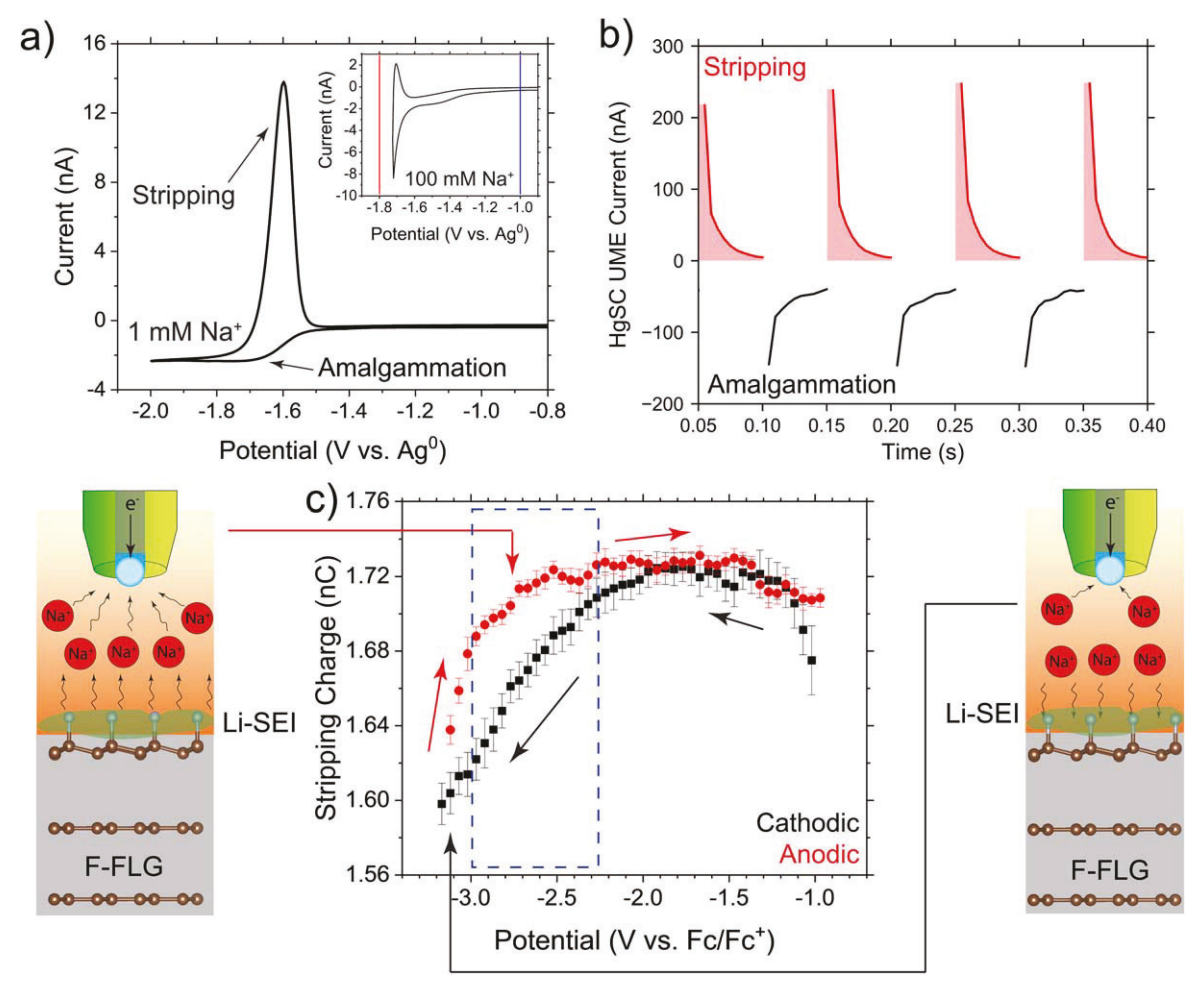


**Figure 3.** Ion-sensitive scanning electrochemical microscopy for tracking Na<sup>+</sup> fluxes. (a) Amalgammation and stripping behavior of HgSC in dilute 1 mM Na<sup>+</sup> concentrations, with inset revealing HgSC response at 100 mM Na<sup>+</sup> concentration. Identification of amalgamation (red line) and stripping potentials (blue line) for chronoamperometric measurement is shown in the inset Figure. (b) Initial chronoamperometric pulses at a fixed substrate potential illustrating calculation of stripping charge (shaded region), with full chronoamperometric data shown in Fig. S17. (c) Variation of Na<sup>+</sup> stripping charge from the HgSC as a function of potential applied at the F-FLG substrate. The schematics show how stripping charge decreases/increases depending on Na<sup>+</sup> being drawn in and out of F-FLG. The blue box highlights the potential regime associated with charge storage process, same as the red box in Fig. 2c. All SECM measurements were performed with a F-FLG electrode with a preconditioned Li-based SEI in 0.1 M NaPF<sub>6</sub> in PC:EC. Fc/Fc<sup>+</sup> was used as an internal standard for the reference potential.

type intercalation mechanisms or other processes such as adsorption (known to occur with  $\mathrm{Na}^+$  charge storage in other carbon structures such as hard carbon).  $^{50,51}$ 

We verified that these reversible peaks were not observable in non-fluorinated FLG anodes with a preformed Li-based SEI, as shown in Fig. 2d. These observations indicate both fluorination and preformed Li-based SEIs are integral for reversible Na<sup>+</sup> charge storage to take place. Interestingly, the use of fluorinated additives such as fluor-oethylene carbonate in conjunction with NaPF<sub>6</sub> salts have been reported to improve cycling performance and SEI characteristics with hard carbon anodes. <sup>52,53</sup> These observations indicate the presence of kinetic barriers towards Na<sup>+</sup> charge storage can be overcome with fluorinated interphases. While our CV and galvanostatic (dis)charge measurements indicate electrochemically reversible processes taking place, there is no direct evidence of this phenomenon being associated with Na<sup>+</sup> intercalation. To first prove the participation of Na<sup>+</sup> in this process, we utilized ion-sensitive SECM measurements.

Ion-sensitive SECM measurements performed in this study utilized Hg sphere-capped UME tips (HgSCs) positioned  $\sim 6~\mu m$  from F-FLG, subsequently referred as the substrate (Fig. S16). Na<sup>+</sup> uptake and release from the substrate was tracked through stripping at the HgSC tip via SECM redox competition mode. <sup>54–56</sup> A recently developed chronoamperometric pulsing protocol <sup>56,57</sup> was applied at the tip to track Na<sup>+</sup> fluxes while preventing Hg oversaturation. <sup>56</sup> An

ideal amalgamation/stripping response of  $\mathrm{Na^+}$  with HgSCs is shown in Fig. 3a, with the oversaturated response presented inset. Elaborating on this method, we first utilized tip CVs to locate amalgamation and stripping of  $\mathrm{Na^+}$  at  $-1.8\,\mathrm{V}$  and  $-1.0\,\mathrm{V}$  vs Ag wire quasireference (QRE) (Fig. 3a inset). Subsequently, we performed a double chronoamperometric measurement (consisting of 30 amalgamation and stripping pulses each of 0.05 s to prevent oversaturation) while varying the substrate's potential in steps of 50 mV. The local concentration of  $\mathrm{Na^+}$  is indirectly indicated by the average stripping charge, and fluxes are indicated by changes in the stripping charge at different substrate potentials. Figure 3b highlights the integrated region from the stripping pulses, which are averaged across the 30 pulses (Fig. S17).

Ion-sensitive SECM data in Fig. 3c highlighted a clear uptake and release of  $\mathrm{Na}^+$  at a potential window between -2 and -3.2 V. This reversible flux correlates well with the electrochemical process associated with peak (ii) in Fig. 2c, confirming the involvement of  $\mathrm{Na}^+$  in charge storage. Interestingly, we note that there is a minor deviation ( $\sim$ 0.02 nC) from the baseline charge values at -1.5 V to -1.0 V (Fig. 3c), indicating a low flux of  $\mathrm{Na}^+$  being consumed by the substrate. This electrochemical activity corresponds to peak (i) indicated in Fig. 1c, highlighting its association with  $\mathrm{Na}^+$ .

CV and SECM measurements suggest reversible Na<sup>+</sup> charge storage to be taking place in F-FLG, but a structurally-sensitive

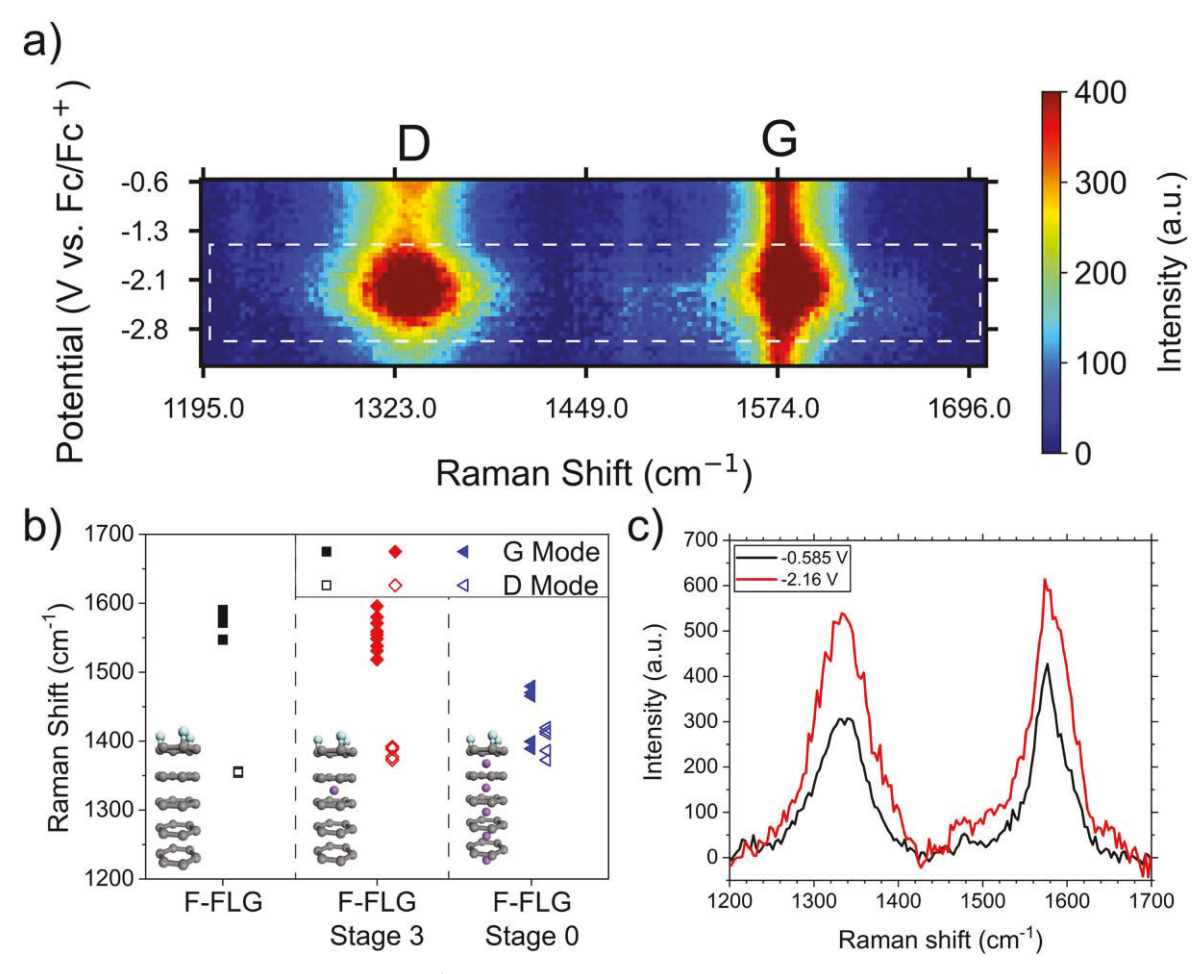


**Figure 4.** In situ Raman spectroscopic measurements of Na<sup>+</sup> intercalation. (a) Heat map of Raman intensities illustrating changes in D and G peaks during CV in the cathodic sweep, with white box depicting potential regime associated with charge storage process. (b) Summary of vibrational modes in Raman for the different structures shown inset. Animated modes are included under Figs. S4–S9. (c) Raman spectra at the beginning of the CV  $(-0.585 \text{ V vs Fc/Fc}^+)$  and at  $-2.16 \text{ V vs Fc/Fc}^+$ .

technique is required to discern between intercalation and adsorption. Therefore, we resorted to in situ Raman spectroscopy which indicates structural distortion of the host based on the vibrational D and G modes of FLG.31,58 Experiments with Raman spectroscopy are challenging given that commercial devices (such as the EL-CELL<sup>51</sup>) typically does not allow solution rinsing, therefore, preforming a Li-based SEI on F-FLG followed by cycling in Naelectrolyte is considerably difficult. Additional difficulties arise in controlling potentials as the ELCell utilizes a two-electrode setup, making correlation to our three-electrode analytical experiments a challenge. Therefore, we constructed a sealed teflon cell in-house, equipped for performing three-electrode measurements with a bare PPyQRE reference and Pt counter electrode (Fig. S18, S19 shows schematics and pictures of the in situ cell respectively). This setup enabled the formation of a Li-based SEI, followed by subsequent cycling in Na electrolyte. Raman data shown in Fig. 4 was obtained from the back-side of the F-FLG electrode. This is a unique feature of our ultra-thin electrodes, which enable the Raman investigation without having to go directly through the electrolyte or the SEI. CVs from cycling the sealed Raman cell inside a glovebox was observed to be slightly different from those obtained outside (Fig. S20), likely due to some air and/or moisture intrusion. Nevertheless, the voltammograms in Fig. S20 possessed an anodic peak between -2.7 to -2.0 V, matching the observations in Fig. 2c. Subsequently, we analyzed the spectra collected in the experiment, after post processing to remove baselines and perform peak fits, using a Python script (details in Fig. S21).

The heat map in Fig. 4a illustrates the evolution in Raman D and G bands of F-FLG during the cathodic sweep in CV. An increase in peak widths of the D and G peaks is clearly observed, starting from -1.7 V, (Fig. S22) which is an indicator of ion-intercalation processes. 51 However, we did not observe any change in the G peak position, contrary to what is reported during Li<sup>+</sup> intercalation at FLG and Na<sup>+</sup> intercalation in hard carbon. <sup>31,51</sup> Therefore, to interpret the in situ Raman results, we turned to simulations of the D and G Raman modes, shown in Fig. 4b. We observed that complete intercalation of Na+ in fluorinated four-layer graphene does lead to the G peaks shifting to lower wavenumbers. This observation is in agreement with simulations in our previous work<sup>3</sup> with  $\mathrm{Li}^+$  and  $\mathrm{K}^+$  intercalation on FLG predicted a  $\sim \! 100\,\mathrm{cm}^{-1}$ blueshift for the G peak, with experimental observations confirming this effect with a  $\sim 70 \, \text{cm}^{-1}$  shift during the formation of stage 1 intercalated structures. Thus, we are aware that the extent of blueshift suggested by Fig. 4b for the intercalated structures with high occupancy is possible. However, our voltammetry data in Fig. 2 highlighted that a Stage 0 intercalated structure (NaC<sub>6</sub>) was never attained, instead NaC<sub>14-18</sub> stoichiometries (~3 times lesser Na<sup>+</sup> content) were observed in F-FLG. Therefore, it is plausible that dilute intercalation structures (analogous to Stage 3) formed, whose Raman bands are presented in Fig. 4b, and we could not verify if the predicted  $\sim$ 100 cm<sup>-1</sup> blueshift will take place owing to NaC<sub>6</sub> type structures forming in F-FLG. These Raman peaks revealed no shift in the G peak position, rather additional peaks in the 1500–1600 cm<sup>-1</sup> region were predicted, which will result in G peak broadening, consistent with our

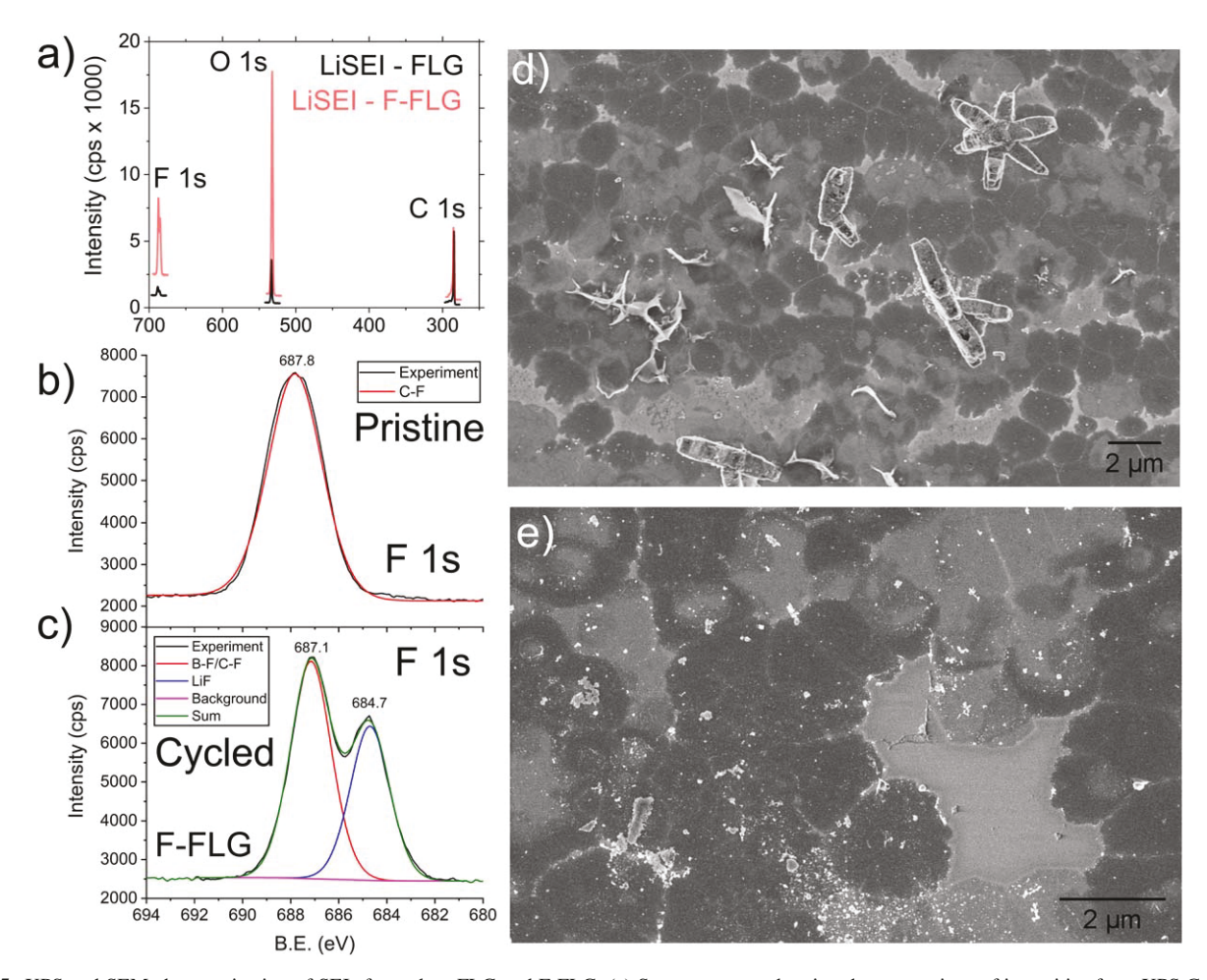


**Figure 5.** XPS and SEM characterization of SEIs formed on FLG and F-FLG. (a) Survey spectra showing the comparison of intensities from XPS C 1 s, O 1 s and F 1 s signals. Peak fitting of F 1 s spectra for (b) pristine and (c) cycled F-FLG samples. (d) and (e) SEM micrographs of Li-based SEI on FLG and F-FLG respectively

experimental data in Figs. 4a and 4c. The experimental data also shows the D peak slightly moving towards higher wavenumbers (Figure S23), as observed in the simulation in Fig. 4b. Additionally, the experimental observation of D peak broadening and some signal intensity in the 1480–1520 cm<sup>-1</sup> region between -2.1 to -2.8 V, matched simulations of Raman peaks from a different Stage 3 structure (Fig. S24). SEI species do not show up in these in situ Raman experiments, as shown in Fig. S25. These correlations of our experiment with simulated structures provided strong evidence that a Na<sup>+</sup> intercalation process is taking place in the F-FLG anode.

In situ Raman data in the anodic sweep (Fig. S26a) revealed a decrease in the G and D peak intensities, followed by a subsequent increase. While reasons behind this asymmetric behavior during cycling are unclear, we observed that the G peak position did not return to original values (Fig. S26b) over the course of the CV. This observation indicates that there are structural changes taking place in F-FLG during cycling in Na<sup>+</sup> electrolyte. Additionally, in a separate control experiment, we observed significant loss of Li<sup>+</sup> intercalation capacity after cycling an F-FLG electrode with preformed SEI in Na<sup>+</sup> electrolyte (Fig. S27), indirectly adding evidence that the graphene structure changes during the Na<sup>+</sup> intercalation.

In summary, our measurements with CV, ion-sensitive SECM and in situ Raman spectroscopy provide collective evidence of Na + intercalation taking place in F-FLG structures. These experimental observations therefore indicate that our earlier theoretical calculations have practical basis, and surface functionalization may enable Na<sup>+</sup> intercalation by tailoring interactions between guest and host species. In addition, it has been reported previously that fluorination

via XeF<sub>2</sub> can expand the interlayer spacing of graphene layers,<sup>59</sup> which is something that we have observed through simulations (Fig. S28), albeit to a slight extent. Any expansion in interlayer spacing may influence Na<sup>+</sup> intercalation, as illustrated in other work with Janus graphene structures.<sup>60</sup>

Finally, we utilized ex situ XPS and SEM to characterize the composition and morphology of the interphases formed on FLG and F-FLG with preformed Li-SEI. The F-FLG sample exhibits similar C 1 s intensities compared to FLG, but markedly different F 1 s and O 1 s signals after cycling in Na-electrolyte, as shown in Fig. 5a. To understand the evolution of fluorinated phases in F-FLG, we performed peak fitting of the F 1 s signals on pristine and cycled samples, as shown in Figs. 5b and 5c. Peak fitting of the F 1 s signals (Figs. 5b and 5c) indicates LiF formation after cycling at 684.7 eV, along with contributions from fluorinated carbon species at 687.8 eV. However, the peak at 687.1 eV likely comprises of contributions from B-F species present in the SEI, that have been observed previously on graphene anodes at binding energies slightly lesser than 687 eV. <sup>56</sup>

Comparing fluorinated species on cycled FLG and F-FLG anodes revealed that both SEIs comprised of LiF species; C-F and/or B-F maybe present in the FLG anodes (Fig. S29). The O 1 s spectra in Fig. S30 shows signals from Li<sub>2</sub>CO<sub>3</sub> (confirmed by C 1 s and Li 1 s spectra, Figures S31, S32), which was not observed in the SEI on FLG sample. However, given the ex situ nature of the measurement, it is plausible that the carbonates arose due to air exposure. The XPS also revealed the thin nature of the SEI, with signals from underlying SiO<sub>2</sub> visible (Fig. S33). While the true composition of the SEI

interphases cannot be discerned from ex situ XPS, the differences in fluorinated content between the F-FLG and FLG samples are unambiguous. This observation ties well with a general trend of fluorinated interphases being beneficial for LIB and NIB anodes. 61,62

SEM micrographs in Fig. 5d, e confirmed the thin nature of the SEIs formed, with underlying graphene being observable through the interphases on both FLG and F-FLG anodes. The F-FLG anode exhibits interphases composed of sub-micron particulates, whereas the FLG anode revealed well-defined, scattered, solid structures  $>1 \mu m$  in size. These particles maybe arising from artifacts given the ex situ nature of the measurement. In contrast to the thick SEI formed with NaPF<sub>6</sub> on F-FLG with no preformed Li-based SEI (Fig. S10), both the Li-SEI modified FLG and F-FLG electrodes show no dense deposits. XPS shows little incorporation of Na (Fig. S34) inside the F-FLG interphase, likely due to the dissolution of Na-SEI components during rinsing, as reported in literature.<sup>8,63–65</sup> Overall, the data in Fig. 5 shows that SEI is present in all surfaces that underwent cycling, whether fluorinated or not, as SEI formation takes place before intercalation. At present we cannot distinguish if there are domains with different SEI coverage and compositions. Despite these caveats, XPS and SEM data indicated that changes in the SEI composition likely played a role in achieving reversible Na<sup>+</sup> intercalation on F-FLG.

### Conclusions

Our measurements with F-FLG conclusively revealed the critical role that surface modification and subsequent interphase formation have in enabling reversible intercalation of Na<sup>+</sup> in graphitic materials. Ion-sensitive SECM was able to confirm the participation of Na<sup>+</sup> in charge storage, and in situ Raman measurements indicated a Stage-3 type intercalation structure forming during cycling. While simulations revealed Na+ intercalated four-layer fluorinated graphene structures were thermodynamically favorable, our electrochemical experiments and in situ and ex situ characterization revealed that the interphase formed on F-FLG in Na electrolyte was not sufficient for Na<sup>+</sup> intercalation in the graphitic host. Instead, a preformed Li-based SEI on F-FLG was required for attaining reversible intercalation. Since fluorination of FLG was necessary to observe Na<sup>+</sup> intercalation, our results revealed the dual role that fluorination may exhibit towards this process, either for improving SEI properties for Na+ ion transfer and for stabilizing the intercalated structure. In summary, our approach using FLG electrodes shows promise as a platform for investigating intercalation processes for beyond Li-ion type systems. We also highlight surface modification as a potential strategy for enabling charge storage in thermodynamically unfavorable systems. These strategies may hold relevance in energy storage devices such as supercapacitors or batteries with thin film, nanostructured, or nanoparticle electrodes. Future work is required in the domain of materials engineering for evaluating the surface modifier approach in graphitic carbon materials with greater intercalation capacity for applications in technologically relevant devices.

# Acknowledgments

The research reported here was funded by NSF DMR Award 1905803. J.S. and A.M.v.d.Z were supported by the National Science Foundation through the University of Illinois Urbana-Champaign Materials Research Science and Engineering Center DMR-1720633. The authors acknowledge the use of facilities and instrumentation supported by NSF through the University of Illinois Materials Research Science and Engineering Center DMR-1720633. CVD synthesis, SEM, XPS, and Raman measurements were carried out in the Materials Research Laboratory Central Research Facilities, University of Illinois. We acknowledge central facilities at the Holonyak Micro & Nanotechnology Laboratory, and the Beckman Institute, University of Illinois, for graphene fluorination, sputter coating, and optical transmittance and in situ Raman measurements. We also acknowledge David Williams and the

School of Chemical Sciences Machine Shop for assistance with the in situ Raman cell design. D.S. also thanks Dr Michael J. Counihan and Michael Pence for helping with the in situ Raman cell setup and experiments. The computational part of this work was carried out was supported in part through computational resources and services provided by the Institute for Cyber-Enabled Research at Michigan State University.

#### **ORCID**

Dipobrato Sarbapalli https://orcid.org/0000-0001-7281-4474 Yu-Hsiu Lin https://orcid.org/0000-0002-3599-9032 Sean Stafford https://orcid.org/0000-0001-8010-4202 Abhiroop Mishra https://orcid.org/0000-0003-3403-4455 Jingshu Hui https://orcid.org/0000-0002-6987-4414 A Nijamudheen (b) https://orcid.org/0000-0001-9191-1851 Adolfo I. B. Romo https://orcid.org/0000-0002-9288-2420 Zachary T. Gossage https://orcid.org/0000-0003-3745-2919 Arend M. van der Zande (b) https://orcid.org/0000-0001-5104-9646 Jose L. Mendoza-Cortes https://orcid.org/0000-0001-5184-1406 Joaquín Rodríguez-López https://orcid.org/0000-0003-4346-4668

#### References

- 1. L. Trahey et al., Proc. Natl Acad. Sci., 117, 12550 (2020).
- 2. C. Xu, Q. Dai, L. Gaines, M. Hu, A. Tukker, and B. Steubing, Commun. Mater., 1,
- 3. M. Weil, S. Ziemann, and J. Peters, Behaviour of Lithium-Ion Batteries in Electric Vehicles: Battery Health, Performance, Safety, and Cost, ed. G. Pistoia and B. Liaw (Springer, Cham) p. 59 (2018).
- 4. K. Chayambuka, G. Mulder, D. L. Danilov, and P. H. L. Notten, Adv. Energy Mater., 10, 2001310 (2020).
- 5. M. K. M. Mann, T. Ahmad, and M. Steward Darlene, Vehicle Technologies Office Annual Merit Review and Peer Evaluation Meeting (Washington, D.C) (2018), https://www.osti.gov/biblio/1529215.
- 6. Y.-S. Hu and Y. Lu, ACS Energy Lett., 4, 2689 (2019).
- K. Kubota, M. Dahbi, T. Hosaka, S. Kumakura, and S. Komaba, Chem. Rec., 18, 459 (2018).
- 8. N. Yabuuchi, K. Kubota, M. Dahbi, and S. Komaba, Chem. Rev., 114, 11636 (2014).
- 9. K. M. Abraham, ACS Energy Lett., 5, 3544 (2020).
- 10. A. Scott, C & EN Global Enterprise, 100, 16 (2022).
- 11. K. Kubota, S. Kumakura, Y. Yoda, K. Kuroki, and S. Komaba, Adv. Energy Mater., 8, 1703415 (2018).
- 12. A. Patra, J. Davis, S. Pidaparthy, H. Karigerasi Manohar, B. Zahiri, A. Kulkarni Ashish, A. Caple Michael, P. Shoemaker Daniel, M. Zuo Jian, and V. Braun Paul, Proc. Natl Acad. Sci., 118, e2025044118 (2021).
- 13. D. Kundu, E. Talaie, V. Duffort, and L. F. Nazar, Angew. Chem. Int. Ed., 54, 3431 (2015).
- 14. S. Komaba, W. Murata, T. Ishikawa, N. Yabuuchi, T. Ozeki, T. Nakayama, A. Ogata, K. Gotoh, and K. Fujiwara, Adv. Funct. Mater., 21, 3859 (2011).
- 15. M. Á. Muñoz-Márquez, D. Saurel, J. L. Gómez-Cámer, M. Casas-Cabanas, E. Castillo-Martínez, and T. Rojo, Adv. Energy Mater., 7, 1700463 (2017).
- 16. D. A. Stevens and J. R. Dahn, J. Electrochem. Soc., 147, 1271 (2000).
- 17. A. Kamiyama, K. Kubota, T. Nakano, S. Fujimura, S. Shiraishi, H. Tsukada, and S. Komaba, ACS Appl. Energy Mater., 3, 135 (2020).
- 18. A. Eldesoky, M. Bauer, S. Azam, E. Zsoldos, W. Song, R. Weber, S. Hy, M. B. Johnson, M. Metzger, and J. R. Dahn, J. Electrochem. Soc., 168, 110543 (2021).
- 19. C. Zhao, Y. Lu, J. Yue, D. Pan, Y. Qi, Y.-S. Hu, and L. Chen, J. Energy Chem., 27,
- 20. Y. Zhao, K. R. Adair, and X. Sun, Energy Environ. Sci., 11, 2673 (2018).
- 21. D. A. Stevens and J. R. Dahn, J. Electrochem. Soc., 148, A803 (2001).
- 22. J. R. Dahn, T. Zheng, Y. Liu, and J. S. Xue, Science, 270, 590 (1995).
- 23. R. Fong, U. von Sacken, and J. R. Dahn, J. Electrochem. Soc., 137, 2009 (1990). 24. A. Nijamudheen, D. Sarbapalli, J. Hui, J. Rodríguez-López, and J. L. Mendoza-Cortes, ACS Appl. Mater. Interfaces, 12, 19393 (2020).
- 25. H. Moriwake, A. Kuwabara, C. A. J. Fisher, and Y. Ikuhara, RSC Adv., 7, 36550
- G. Yoon, H. Kim, I. Park, and K. Kang, Adv. Energy Mater., 7, 1601519 (2017).
  J. Son et al., Adv. Mater., 31, 1903424 (2019).
- 28. J. Son et al., Nat. Commun., 9, 3988 (2018).
- 29. J. Hui, M. Burgess, J. Zhang, and J. Rodríguez-López, ACS Nano, 10, 4248 (2016).
- 30. J. Hui, A. Nijamudheen, D. Sarbapalli, C. Xia, Z. Qu, J. L. Mendoza-Cortes, and J. Rodríguez-López, *Chem. Sci.*, **12**, 559 (2021).
- 31. J. Hui, N. B. Schorr, S. Pakhira, Z. Qu, J. L. Mendoza-Cortes, and J. Rodríguez-López, J. Am. Chem. Soc., 140, 13599 (2018).
- 32. J. D. Wood et al., Nanotechnol., 26, 055302 (2015).
- 33. R. R. Nair, P. Blake, A. N. Grigorenko, K. S. Novoselov, T. J. Booth, T. Stauber, N. M. R. Peres, and A. K. Geim, Science, 320, 1308 (2008).
- 34. J. T. Robinson et al., Nano Lett., 10, 3001 (2010).
- 35. J. Ghilane, P. Hapiot, and A. J. Bard, Anal. Chem., 78, 6868 (2006).

- 36. D. Sarbapalli, A. Mishra, and J. Rodríguez-López, Anal. Chem., 93, 14048 (2021).
- 37. X. Dou, I. Hasa, D. Saurel, C. Vaalma, L. Wu, D. Buchholz, D. Bresser, S. Komaba, and S. Passerini, Mater. Today, 23, 87 (2019).
- 38. Z. J. Barton and J. Rodríguez-López, Anal. Chem., 86, 10660 (2014).
- 39. Z. J. Barton and J. Rodríguez-López, Anal. Chem., 89, 2708 (2017).
- 40. R. S. Dovesi et al., Crystal14 User's Manual (2014), https://www.afrl.hpc.mil/ software/info/crystal/crystal14.pdf.
- 41. R. Dovesi et al., WIREs Computational Molecular Science, 8, e1360 (2018).
- 42. S. H. Vosko, L. Wilk, and M. Nusair, Can. J. Phys., 58, 1200 (1980).
- 43. S. Grimme, J. Antony, S. Ehrlich, and H. Krieg, J. Chem. Phys., 132, 154104 (2010).
- 44. S. Grimme, S. Ehrlich, and L. Goerigk, J. Comput. Chem., 32, 1456 (2011).
- 45. M. F. Peintinger, D. V. Oliveira, and T. Bredow, J. Comput. Chem., 34, 451 (2013).
- 46. P. Pulay, Chem. Phys. Lett., 73, 393 (1980).
- 47. P. Pulay, J. Comput. Chem., 3, 556 (1982).
- 48. A. Metrot, D. Guerard, D. Billaud, and A. Herold, Synth. Met., 1, 363 (1980).
- 49. W. C. Sleppy, Inorg. Chem., 5, 2021 (1966).
- 50. D. Saurel, B. Orayech, B. Xiao, D. Carriazo, X. Li, and T. Rojo, Adv. Energy Mater., 8, 1703268 (2018).
- 51. J. S. Weaving, A. Lim, J. Millichamp, T. P. Neville, D. Ledwoch, E. Kendrick, P. F. McMillan, P. R. Shearing, C. A. Howard, and D. J. L. Brett, ACS Appl. Energy Mater., 3, 7474 (2020).
- 52. A. Bouibes, N. Takenaka, T. Fujie, K. Kubota, S. Komaba, and M. Nagaoka, ACS Appl. Mater. Interfaces, 10, 28525 (2018).

- 53. M. Dahbi, T. Nakano, N. Yabuuchi, S. Fujimura, K. Chihara, K. Kubota, J.-Y. Son, Y.-T. Cui, H. Oji, and S. Komaba, ChemElectroChem, 3, 1856 (2016).
- 54. Z. T. Gossage, J. Hui, D. Sarbapalli, and J. Rodríguez-López, Analyst, 145, 2631 (2020)
- 55. Z. T. Gossage, J. Hui, Y. Zeng, H. Flores-Zuleta, and J. Rodríguez-López, Chem. Sci., 10, 10749 (2019).
- 56. Y. Zeng, Z. T. Gossage, D. Sarbapalli, J. Hui, and J. Rodríguez-López, ChemElectroChem, 9, e202101445 (2022).
- 57. A. Mishra, D. Sarbapalli, M. S. Hossain, Z. T. Gossage, Z. Li, A. Urban, and J. Rodriguez-Lopez, J. Electrochem. Soc., 169, 086501 (2022).
- 58. J. Zou, C. Sole, N. E. Drewett, M. Velický, and L. J. Hardwick, J. Phys. Chem. Lett., 7, 4291 (2016).
- 59. J. Son et al., Nano Lett., 21, 891 (2021).
- 60. J. Sun, M. Sadd, P. Edenborg, H. Grönbeck, P. H. Thiesen, Z. Xia, V. Quintano, R. Qiu, A. Matic, and V. Palermo, Sci. Adv., 7, eabf0812 (2021).
- 61. C. Wang, Y. S. Meng, and K. Xu, J. Electrochem. Soc., 166, A5184 (2018).
- 62. A. Nimkar, N. Shpigel, F. Malchik, S. Bublil, T. Fan, T. R. Penki, M. N. Tsubery, and D. Aurbach, ACS Appl. Mater. Interfaces, 13, 46478 (2021).
- 63. L. A. Ma, A. J. Naylor, L. Nyholm, and R. Younesi, Angew. Chem. Int. Ed., 60, 4855 (2021).
- 64. M. Dahbi, N. Yabuuchi, K. Kubota, K. Tokiwa, and S. Komaba, Phys. Chem. Chem. Phys., 16, 15007 (2014).
- 65. J. Song, B. Xiao, Y. Lin, K. Xu, and X. Li, Adv. Energy Mater., 8, 1703082 (2018).